Structured illumination microscopy with noise-controlled image reconstructions

Smith, Carlas S.; Slotman, Johan A.; Schermelleh, Lothar; Chakrova, Nadya; Hari, Sangeetha; Vos, Yoram; Hagen, Cornelis W.; Houtsmuller, Adriaan B.; Hoogenboom, Jacob P.; Stallinga, Sjoerd

Important note
To cite this publication, please use the final published version (if applicable).
Please check the document version above.

Check for updates

Structured illumination microscopy with noise-controlled image reconstructions

Carlas S. Smith [1,2], Johan A. Slotman [3], Lothar Schermelleh [4], Nadya Chakrova[1], Sangeetha Hari[1], Yoram Vos[1], Cornelis W. Hagen[1], Marcel Müller [5], Wiggert van Cappellen [3], Adriaan B. Houtsmuller[3], Jacob P. Hoogenboom [1] and Sjoerd Stallinga [1]✉

Super-resolution structured illumination microscopy (SIM) has become a widely used method for biological imaging. Standard reconstruction algorithms, however, are prone to generate noise-specific artifacts that limit their applicability for lower signal-to-noise data. Here we present a physically realistic noise model that explains the structured noise artifact, which we then use to motivate new complementary reconstruction approaches. True-Wiener-filtered SIM optimizes contrast given the available signal-to-noise ratio, and flat-noise SIM fully overcomes the structured noise artifact while maintaining resolving power. Both methods eliminate ad hoc user-adjustable reconstruction parameters in favor of physical parameters, enhancing objectivity. The new reconstructions point to a trade-off between contrast and a natural noise appearance. This trade-off can be partly overcome by further notch filtering but at the expense of a decrease in signal-to-noise ratio. The benefits of the proposed approaches are demonstrated on focal adhesion and tubulin samples in two and three dimensions, and on nanofabricated fluorescent test patterns.

SIM is a super-resolution technique that offers twofold increased spatial resolution along two or three dimensions plus optical sectioning with strongly enhanced contrast compared with conventional widefield fluorescence microscopy using uniform illumination[1–6], and is compatible with live cell imaging[7–9]. Further reduction of resolution below the 100 nm length scale can be achieved by making use of the nonlinear fluorescence response[10–13]. Current image reconstruction methods[3,4,14–16] depend on ad hoc tuneable parameters and are susceptible to various types of artifact[17,18]. The effort to distinguish 'real' structural resolution improvement from noise-related deconvolution artifacts in SIM has recently inspired much controversy in the field[19,20]. The root causes of this confusion are (1) the lack of insight into the mechanism of image formation that requires a reconstruction procedure of considerable mathematical complexity, (2) the use of ad hoc parameters with large effect on the final image but with unclear physical meaning and (3) the absence of an unambiguous method to separate true signal from noise.

Here we address these issues first by an in-depth analysis of the propagation of noise through the image reconstruction chain of state-of-the-art linearly filtered SIM. We use this to explain the structured noise artifact of SIM, the amplification of noise structures at intermediate length scales at low signal conditions. In particular, the analysis clarifies the role of ad hoc filtering operations such as regularization. In a next step, the understanding of noise propagation is applied in new SIM reconstruction methods. These methods are designed for optimizing contrast or a natural noise appearance, and to eliminate ad hoc reconstruction parameters. The underlying goal is to make the representation of objects in SIM images as objective as possible.

Results

Propagation of noise through the image reconstruction chain of SIM. The goal of image reconstruction is to provide an estimate e_k^{rec} (with $k = 1, \cdots, N$ the index denoting the different pixels) of the underlying fluorescent object f_k. This estimate depends linearly on the images acquired for the M_r different rotations and M_t different translations of the illumination pattern via a sequence of Fourier (spatial frequency) space manipulations (Supplementary Note 1). The reconstructed object e_k^{rec} is a sum of a term e_k that corresponds to the reconstruction in the absence of noise and a perturbation δe_k of that ideal reconstruction due to noise. The Fourier transforms (FTs) of e_k and δe_k are denoted as $\hat{e}_j$ and $\delta\hat{e}_j$, respectively, where the hat indicates the FT and the index j indicates the Fourier pixel with spatial frequency $\vec{q}_j$.

The signal power and the noise variance in Fourier space $\hat{S}_j \equiv |\hat{e}_j|^2$ and $\hat{N}_j \equiv \langle |\delta\hat{e}_j|^2 \rangle$ are used here to quantify the noise and signal level. The noise variance can be determined empirically by making K repeated acquisitions of a fixed specimen, and computing the variance over the K reconstructions in Fourier space. We have analyzed the propagation of noise through the reconstruction chain (full theory in Supplementary Note 2) and found analytical expressions for the signal power and noise variance:

$$\hat{S}_j = \frac{\hat{A}_j^2 \hat{D}_j^2}{\left[\hat{w}_j + \hat{D}_j\right]^2} \left|\hat{f}_j\right|^2 \tag{1}$$

$$\hat{N}_j = \frac{\hat{A}_j^2}{\left[\hat{w}_j + \hat{D}_j\right]^2} \left(\hat{f}_0 \hat{V}_j + N\sigma^2 \hat{D}_j\right) \tag{2}$$

[1]Department of Imaging Physics, Delft University of Technology, Delft, the Netherlands. [2]Department of Physiology, Anatomy and Genetics, Centre for Neural Circuits and Behaviour, University of Oxford, Oxford, UK. [3]Department of Pathology, Erasmus Optical Imaging Centre, Erasmus Medical Center, Rotterdam, the Netherlands. [4]Micron Advanced Bioimaging Unit, Department of Biochemistry, University of Oxford, Oxford, UK. [5]Biochemistry, Molecular and Structural Biology Section, Leuven University, Leuven, Belgium. ✉e-mail: s.stallinga@tudelft.nl

Here $\hat{f}_j$ is the spatial-frequency spectrum of the underlying fluorescent object, $\hat{f}_0 \equiv \sum_{k=1}^{N} \hat{f}_k$ is the sum fluorescence signal, $\hat{A}_j$ is the apodization filter[21], which has a low-pass character for avoiding halo, negative pixel and edge ringing artifacts, $\hat{w}_j$ is the regularization filter and σ is the root-mean-square camera readout noise. State-of-the-art SIM reconstructions use a regularization filter that is chosen ad hoc to be independent of spatial frequency ($\hat{w}_j = w$ for all $\mathbf{q}_j$). The functions $\hat{D}_j$ and $\hat{V}_j$ are sums over the M_r rotations and over the set $\mathbb{M}$ of nonzero Fourier orders of the periodic illumination pattern:

$$\hat{D}_j = M_t \sum_{r=1}^{M_r} \sum_{m \in \mathbb{M}} |\hat{a}_m|^2 \left| \hat{g} \left(\mathbf{q}_j - \mathbf{k}_{rm} \right) \right|^2 \qquad (3)$$

$$\hat{V}_j = M_t \sum_{r=1}^{M_r} \sum_{m,m' \in \mathbb{M}} \hat{a}_m \hat{a}_{m'}^* \hat{a}_{m-m'} \hat{g} \left(\mathbf{q}_j - \mathbf{k}_{rm} \right)^*$$
$$\hat{g} \left(\mathbf{q}_j - \mathbf{k}_{rm'} \right) \hat{g} \left(\mathbf{k}_{rm'} - \mathbf{k}_{rm} \right) \qquad (4)$$

where $\hat{g}(\mathbf{q}_j)$ is the microscope's optical transfer function (OTF), $\hat{a}_m$ are the Fourier order strengths and $\mathbf{k}_{rm}$ are the center spatial frequencies of the orders. The noise variance is the sum of contributions due to shot noise and readout noise. For current CMOS (complementary metal oxide semiconductor) or EM-CCD (electron multiplying charged coupled device) cameras, the readout noise is zero or very nearly so. For that reason, we will henceforth neglect the readout noise term. Our theory predicts that, in general, the noise variance is not constant across Fourier space, implying that SIM suffers from spatial-frequency-dependent noise amplification. This is the explanation of the structured noise artifact of SIM.

The noise model also enables assessment of the expected noise power averaged over a neighborhood of a pixel k in real space (Supplementary Note 2). The expected noise power is used to compute the fraction Z_k of the reconstruction that can be attributed to noise in the neighborhood of pixel k. This noise fraction may be used as a feature confidence map, quantifying the effect of noise enhancement in different subregions of the final SIM reconstruction.

In the limit where shot noise is the only noise source, we can also use another noise assessment based on a single SIM acquisition, one that is model independent. The detected photoelectrons in each pixel of the set of raw images are assigned randomly to two new datasets according to a binomial distribution. If the number of photoelectrons per pixel is a statistical variable following Poisson statistics, then it can be shown that the number of photoelectrons per pixel of the two split datasets also follow Poisson statistics[22], and that the two Poisson distributions are independent, implying that the noise in the two split datasets is uncorrelated. By processing the split datasets, two noise-independent SIM reconstructions (at half the average signal level) can be generated. The noise level in the SIM reconstruction derived from the original full dataset can now be assessed from the correlations between the two reconstructions derived from the split data (see Supplementary Note 2 for proofs).

We have tested the theoretical noise analysis by imaging a fixed sample of green fluorescent protein (GFP)-labeled zyxin, a building block of focal adhesions[23], in U2OS cells $K = 10$ times (experimental details in Methods). The signal level is kept low (Fig. 1a,b) to make the effects of noise amplification better visible. Figure 1c–h shows the widefield image and SIM reconstruction for different settings of the regularization parameter w, with clear noise enhancement for small w. Figure 1i–l shows that the noise variance according to our model agrees well with the empirical multi-image noise variance, as well as with the model-independent noise assessment from

processing the split datasets, providing two controls that validate our noise model. The noise enhancement at intermediate spatial frequencies for decreasing w is clearly present. The effect of w on the reconstruction, the noise fraction map that quantifies the level of noise enhancement and the spectral noise variance is shown in Supplementary Video 1.

Figure 1m shows the spectral signal-to-noise ratio[24] $\mathrm{SSNR}_j = \hat{S}_j / \hat{N}_j$ (averaged over rings in Fourier space) as a function of spatial frequency. For the low signal levels in the current experiment, SIM provides a gain over widefield imaging only in the region around the widefield diffraction limit, for length scales larger than about $\lambda/\mathrm{NA} = 382\,\mathrm{nm}$ there is no difference in SSNR. This is attributed to the relatively low effective first-order modulation in view of the nonzero thickness of the sample. The limited improvement due to the low signal level is also shown by the experimental Fourier ring correlation (FRC)[25] curves (Fig. 1j), indicating an improvement in FRC resolution in SIM ($149 \pm 2\,\mathrm{nm}$) over widefield ($239 \pm 2\,\mathrm{nm}$) with a factor of 1.6, and notably less than the extended SIM diffraction limit ($1/(2\mathrm{NA}/\lambda + 2/p) = 103\,\mathrm{nm}$ for the estimated pattern pitch $p = 444\,\mathrm{nm}$), and the diffraction limit for widefield ($\lambda/2\mathrm{NA} = 192\,\mathrm{nm}$), respectively.

Noise-controlled SIM reconstructions. According to our noise propagation model, the SSNR seems to be equal to the product of two factors. The first factor $\left| \hat{f}_j \right|^2 / \hat{f}_0$ depends only on the spatial-frequency spectrum of the underlying object, the fluorescent labeling density and the detected fluorescence brightness. The second factor $\hat{D}_j^2 / \hat{V}_j$ depends only on the imaging system (the microscope OTF and the illumination patterns). The SSNR is independent of the regularization filter $\hat{w}_j$ and of any subsequent apodization filter $\hat{A}_j$. The implication is that several, physically equivalent, choices for these filters can be made, each showing or emphasizing different aspects of image quality, such as contrast or a natural noise appearance, but rooted in exactly the same underlying information content. It is also clear that these different choices cannot tune signal level and contrast independent from the noise appearance.

The first choice of noise-controlled filtering follows the Wiener principle, which optimizes contrast by making the OTF as close as possible to a target OTF (for example the apodization filter), subject to available signal-to-noise ratio. Mathematically, we seek the minimum of the noise averaged quadratic difference between reconstruction and underlying object, low-pass filtered by the target OTF (Supplementary Note 3). This implies a regularization filter:

$$\hat{w}_j = \frac{\hat{V}_j \hat{f}_0}{\hat{D}_j \left| \hat{f}_j \right|^2} = \frac{\hat{D}_j}{\mathrm{SSNR}_j} \qquad (5)$$

that increases with decreasing SSNR, different from state-of-the-art SIM with constant regularization. The key problem in applying true-Wiener filtering is that it requires an estimate of the SSNR from the image itself. The reconstruction $\left| \hat{e}_j + \delta \hat{e}_j \right|^2 = \hat{S}_j + 2\mathrm{Re}\left\{ \hat{e}_j \delta \hat{e}_j^* \right\} + \hat{N}_j$ is a sum of the signal power $\hat{S}_j$, the noise power $\hat{N}_j$ and a signal-noise cross-term. Averaging over rings in spatial-frequency space effectively eliminates the signal-noise cross-term, leaving the sum of signal and noise power. The proposed noise model enables a direct computation of the noise variance $\hat{N}_j$, which can subsequently be used to estimate the signal power $\hat{S}_j$ and the SSNR.

True-Wiener-filtered SIM provides a high-contrast representation of the object, but it suffers, just as state-of-the-art SIM, from an elevated noise level at intermediate spatial frequencies, especially in cases with low photon count or low (effective) modulation of the illumination pattern[18]. The current noise analysis points to a second new reconstruction scheme, one from which this structured noise artifact is eliminated. According to Eq. (2), the spectral noise
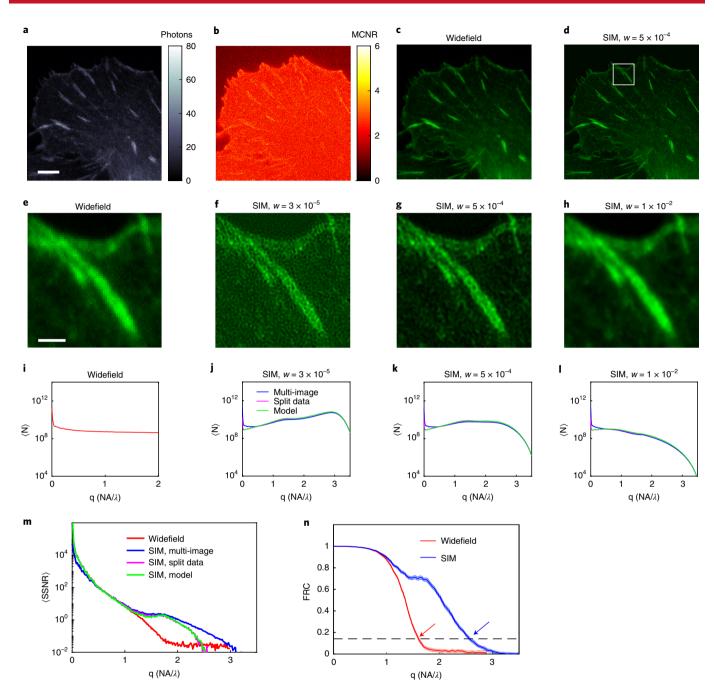
Fig. 1 | Noise propagation in SIM reconstructions. a, Example raw image of a SIM acquisition of GFP-zyxin in focal adhesions. **b**, MCNR, indicating muted stripe contrast due to low signal levels. **c,d**, Widefield and state-of-the-art SIM reconstruction with constant regularization w. **e–h**, Insets of the boxed region in (**d**) showing the widefield image (**e**) and SIM reconstructions with small (**f**), intermediate (**g**) and large (**h**) regularization parameters w. A noise pattern builds up when w is decreased. **i–l**, Measured noise variance $\langle N \rangle$ in Fourier space over the ten independent SIM reconstructions, averaged over rings in Fourier space. **m**, The SSNR determined from ten independent acquisitions for widefield and SIM (and averaged over rings in Fourier space). **n**, FRC curve for widefield and SIM. The intersection of the FRC curves with the resolution threshold 1/7 (dashed curve) gives FRC-resolution values 239 ± 2 nm (widefield, red arrow) and 149 ± 2 nm (SIM, blue arrow) below and above the widefield diffraction limit $\lambda/2\mathrm{NA} = 191$ nm. Scale bar, 5 μm (**a–d**) and 1 μm (**e–h**).

variance can be made independent of spatial frequency by using a regularization filter:

$$\hat{w}_j = \sqrt{\hat{V}_j} - \hat{D}_j \qquad (6)$$

and by discarding the apodization filter altogether ($\hat{A}_j = 1$). This flat-noise SIM reconstruction provides a reconstruction that is independent of the object content and from which all ad hoc tuneable parameters are eliminated, but instead is fully determined by physical parameters only.

The resulting OTF $\hat{g}_j^{\mathrm{SIM}} = \hat{D}_j / \sqrt{\hat{V}_j}$ is a direct measure for the transfer in SSNR from the object to the final flat-noise SIM reconstruction. This can result in a relatively low OTF compared with true-Wiener or state-of-the-art reconstructions, implying a reduced contrast. A mitigation may be found in further notch filtering of the image Fourier orders. This method has been introduced to suppress the two-dimensional (2D)-SIM specific honeycomb artifact
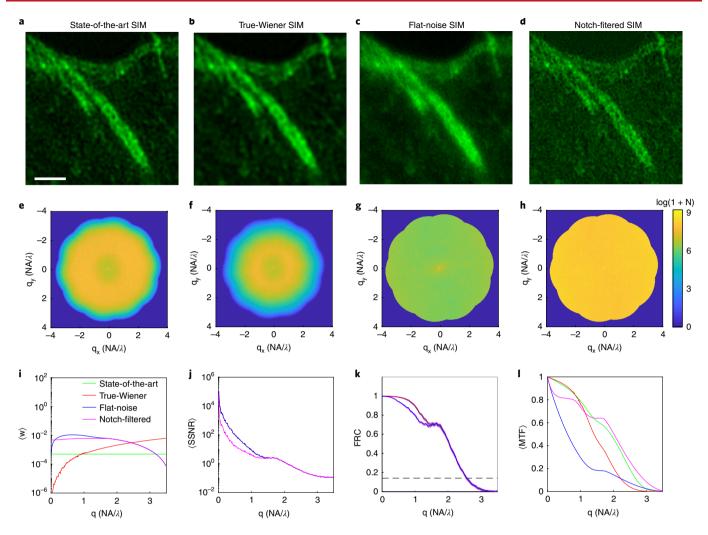
Fig. 2 | Noise-controlled SIM reconstructions. a, State-of-the-art SIM with regularization $w = 5 \times 10^{-4}$. **b–d**, True-Wiener (**b**), flat-noise (**c**) and notch-filtered (**d**) SIM reconstructions for the inset shown in Fig. 1e–h. The two-line substructure is a recognizable true feature, the pronounced small-scale twirls ('hammer finish pattern') is an artifact of reconstructed noise component. **e–h**, Measured noise variance in 2D Fourier space over ten independent SIM reconstructions for state-of-the-art (**e**), true-Wiener (**f**), flat-noise (**g**), and notch-filtered (**h**) SIM. State-of-the-art SIM has a noise ring at medium-to-high spatial frequencies, true-Wiener SIM has a noise ring at lower spatial frequencies, flat-noise SIM has a constant noise plateau and notch-filtered SIM has a constant, but elevated noise plateau. **i**, Regularization parameter (averaged over rings in Fourier space) as a function of spatial frequency. **j**, The SSNR (averaged over rings in Fourier space) for state-of-the-art, true-Wiener and flat-noise SIM is identical. The SSNR for notch-filtered SIM is lower for smaller spatial frequencies. **k**, The FRC curves for state-of-the-art, true-Wiener and flat-noise SIM are identical. The FRC curve for notch-filtered SIM is lower for smaller spatial frequencies. **l**, The MTF (averaged over rings in Fourier space) of the four reconstructions, indicating a lower contrast for flat-noise SIM compared with the other three reconstructions. Scale bar, 1 μm.

and/or background arising from out-of-focus layers[14,16]. Here we use it to optimize image contrast, while keeping the noise spectrum flat. The depth and width of the notch filters per image Fourier order influence the reconstructions functions $\hat{D}_j$ and $\hat{V}_j$ and thereby the flat-noise SIM-OTF (Supplementary Note 3). These notch filter parameters can thus be tuned to minimize the difference between the flat-noise SIM-OTF and a target OTF such as the apodization filter $\hat{A}_j$. This procedure improves the contrast of flat-noise SIM across all spatial frequencies, without introducing any user-adjustable parameters. A drawback is that the overall SSNR level for the lower spatial frequencies is decreased, that is, the overall noise level is higher.

We tested the three proposed noise-controlled reconstructions on the GFP-zyxin datasets of Fig. 1. Figure 2a–c shows the widefield as well as true-Wiener, flat-noise and notch-filtered SIM reconstructions, with Fig. 2d–f showing the corresponding empirical noise variances. Extended Data Fig. 1 shows these reconstructions in combination with the noise fraction maps. True-Wiener

SIM corresponds visually to the optimum regularization setting for state-of-the-art SIM, providing a high-contrast representation and avoiding over- or under-regularization. The structured noise artifact has disappeared in flat-noise SIM, at the expense, however, of a loss in contrast. Notch-filtered SIM fixes the loss in contrast, but at the expense of an increase in overall noise level. The measured spectral noise variances show a noise ring at intermediate spatial frequencies for true-Wiener SIM that is about an order of magnitude higher than the constant plateau for flat-noise SIM. Further evidence for these assessments is provided by the K noise-independent reconstructions and the average of the K reconstructions for the inset (Supplementary Video 2). The regularization parameters, as a function of spatial frequency for true-Wiener and flat-noise SIM shown in Fig. 2g, seem to have low-pass and band-pass character, respectively. The experimental SSNR over the K reconstructions (Fig. 2h) for true-Wiener and flat-noise SIM are identical and higher than the SSNR for notch-filtered SIM at lower spatial
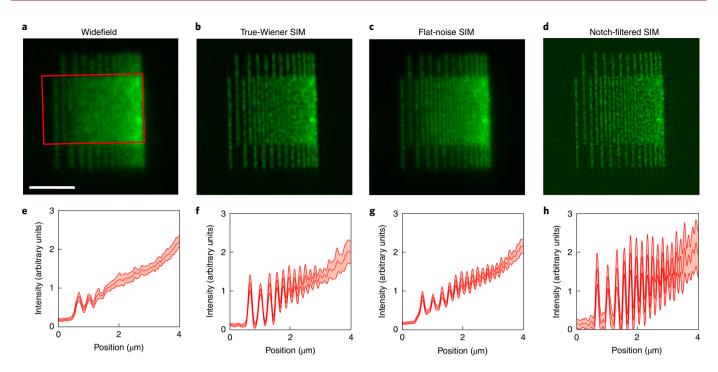
Fig. 3 | Trade-off between noise and contrast in SIM reconstructions. a–d, Widefield (**a**), true-Wiener SIM (**b**), flat-noise SIM (**c**) and notch-filtered SIM (**d**) reconstructions of a chirped nanopatterned structure. **e–h**, Mean and s.d. of the chirped line pattern over the boxed region in **a** for widefield (**e**), true-Wiener SIM (**f**), flat-noise SIM (**g**) and notch-filtered SIM (**h**) reconstructions. Scale bar, 2 μm.

frequencies, and agree reasonably well with the single-image estimates used in the true-Wiener approach. The modulation transfer function (MTF, absolute value of the OTF) for the three reconstructions (Fig. 2h) show a reduced contrast for flat-noise SIM compared with true-Wiener and notch-contrast SIM.

Noise-controlled SIM reconstructions provide representations with strongly reduced noise enhancement in case of poor illumination pattern modulation (Extended Data Fig. 2), in contrast to state-of-the-art SIM. Similar results are also obtained for different illumination patterns than line patterns (Supplementary Note 3), in particular for a system that uses a digital micro-mirror device (DMD) for scanning a multispot array across the sample[26] (Extended Data Fig. 3).

Trade-off between contrast, noise and signal-to-noise. Next, we imaged nanofabricated test structures (experimental details in Methods). Figure 3a–d shows a widefield image and the three noise-controlled SIM reconstructions of a chirped line structure, demonstrating improved resolution of SIM and the trade-offs between contrast, noise level and signal-to-noise ratio between the three new SIM reconstructions. True-Wiener SIM has high contrast at the expense of spatial-frequency dependent noise enhancement. Flat-noise SIM shows two times less noise as quantified by the s.d. along the test object lines of the line response (Fig. 3e–h), but with less contrast. The modulations as a function of line spacing in relation to the noise level point to an identical SSNR and an image resolution of around 160 nm, close to the FRC estimate for the GFP-zyxin sample of Fig. 1. Contrast is restored in notch-filtered SIM, but at the expense of a noise enhancement that is constant over all spatial frequencies. Flat-noise SIM does provide better visibility of very high spatial frequencies, close to the image resolution, as demonstrated on 140 nm pitch line patterns in Extended Data Fig. 4. The trade-offs are also evident from reconstructions of mCherry-CSYCP3 protein in the synaptonemal complex (Extended Data Fig. 5), where the SIM reconstructions resolve the internal two-line structure with line distance of about

200 nm, but differ in modulation, contiguous line structure and background noise.

Noise-controlled SIM reconstructions in three dimensions. So far, results have been shown for 2D-SIM reconstructions of single focal slices of image acquisitions on relatively thin objects. The trade-off between contrast and noise enhancement as in 2D-SIM reconstructions is observed in three-dimensional (3D)-SIM as well, exacerbated by the degree of optical sectioning along the optical axis. Figure 4, Extended Data Fig. 6 and Supplementary Videos 3–6 show full 3D-SIM reconstructions and noise fraction maps of a tubulin sample at different signal levels (Supplementary Fig. 1). Comparison of state-of-the-art SIM with a fixed regularization parameter (Fig. 4b–d) with true-Wiener SIM (Fig. 4e) shows that the SSNR and spatial-frequency-dependent regularization of true-Wiener SIM (Supplementary Fig. 2) results in a reasonable reconstruction for all signal levels, avoiding over and under-regularization in all cases and resulting in a satisfactory MTF (Supplementary Fig. 3). Flat-noise SIM (Fig. 4e) improves resolution, as indicated by the reduction of the width of the tubulin filaments both laterally and axially, and shows no noise amplification. The degree of optical sectioning, however, is poor compared with true-Wiener SIM, making this representation not so valuable for 3D-SIM. This can be improved substantially by contrast-optimized flat-noise SIM using notch filtering (Fig. 4f), albeit at the expense of a small decrease in SSNR (Supplementary Figs. 2 and 3). We have observed similar characteristics of the different noise-controlled SIM reconstructions in SIM images of a bead layer dataset (Extended Data Fig. 7), of a three-color labeled bovine pulmonary artery endothelial cell (BPAEC) (Extended Data Fig. 8 and Supplementary Videos 7), of a two-color labeled C127 cell (Extended Data Fig. 9 and Supplementary Videos 8) and of a live HeLa cell dataset at low signal conditions (Extended Data Fig. 10, Supplementary Fig. 4 and Supplementary Video 9).

Deconvolution and denoising. Richardson–Lucy (RL) deconvolution is known to improve the sharpness of point, line and edge
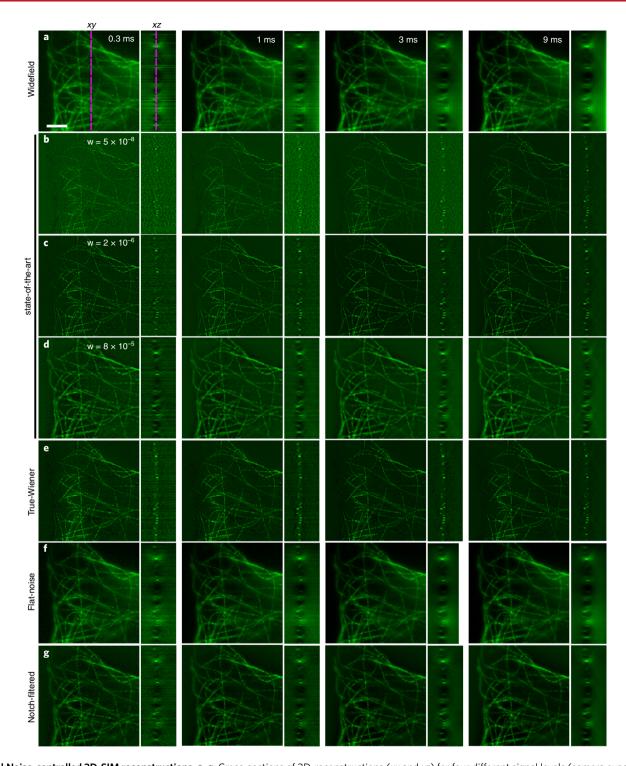
Fig. 4 | Noise-controlled 3D-SIM reconstructions. a–g, Cross-sections of 3D-reconstructions (*xy* and *yz*) for four different signal levels (camera exposure indicated): widefield (**a**); state-of-the-art SIM for small (**b**), intermediate (**c**) and large (**d**) regularization parameters; true-Wiener SIM (**e**); flat-noise SIM (**f**) and notch-filtered SIM (**g**). The dashed lines in **a** indicate the location of the *xz* and *xy* slices. Scale bar, 3 μm.

features in an image, which, depending on the sample, slightly extends the spatial-frequency content above the diffraction limit[27,28]. It is also a suitable benchmark for the noise-controlled linear SIM reconstructions considered so far, as RL-deconvolution is also free from ad hoc user-adjustable parameters. RL-deconvolution is appropriate when the noise on the input images is Poisson-distributed. Flat-noise SIM offers this to a good degree, as opposed to other preprocessed inputs. Figure 5 and Supplementary Fig. 5 show

the results of RL-deconvolution applied to the widefield and the flat-noise SIM reconstructions of the zyxin sample, showing an improvement in resolution in both, which is reflected in slightly better FRC-resolution values (187 ± 2 nm for widefield and 131 ± 3 nm for SIM), but at the expense of noise enhancement, similar to state-of-the-art or true-Wiener SIM. It therefore seems that RL-deconvolution is constrained by the same trade-off between contrast and noise enhancement as linear SIM reconstructions.
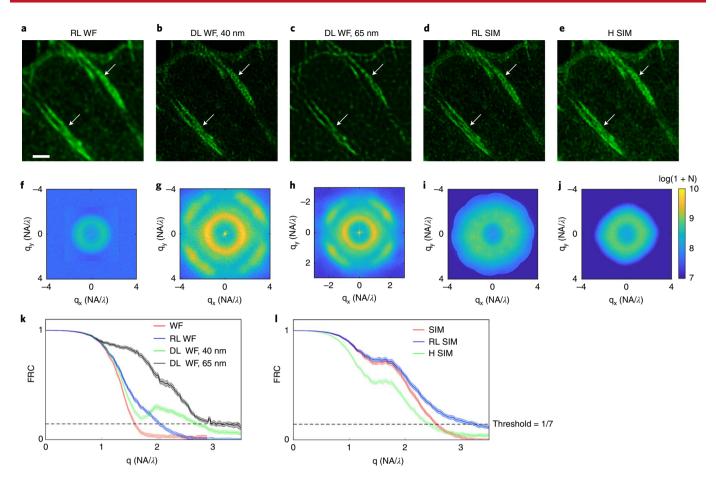
Fig. 5 | Resolution improvement and noise enhancement in deconvolution of GFP-zyxin dataset. a, RL-deconvolution of widefield (WF) image. **b**, DL-deconvolution of widefield image at 40 nm pixel size. **c**, DL-deconvolution of widefield image at 65 nm pixel size. **d**, RL-deconvolution of (flat-noise) SIM image. **e**, H denoised SIM. Arrows indicate features where a significant difference is observed. **f–j**, Spectral noise variance (on a logarithmic scale) over the $K = 10$ independent outcomes of the deconvolution for the RL-WF deconvolution (**f**), the DL-WF deconvolution at 40 nm pixel size (**g**), the DL-WF deconvolution at 65 nm pixel size (**h**), the RL-SIM deconvolution (**i**) and the H-denoised SIM (**j**), showing different types and degrees of noise enhancement. Note the differences in scale for **h** in view of the different pixel size. **k**, FRC curves of widefield based deconvolutions in comparison with the curve for widefield. FRC-resolution improves from 239 ± 2 nm to 187 ± 2 nm (RL), 142 ± 3 nm (DL 40 nm) and 123 ± 6 nm (DL 65 nm). **l**, FRC curves of SIM-based deconvolutions in comparison with the curve for SIM. FRC-resolution changes from 149 ± 1 nm to 131 ± 3 nm (RL) and 159 ± 0.1 nm (H). Scale bar, 1 μm.

We further applied a recent deep learning (DL)-based deconvolution method[29], which is trained to transform widefield images into images with SIM level resolution, to the GFP-zyxin dataset. Figure 5 and Supplementary Fig. 5 show a trade-off between the precision and accuracy of this method, pointing to limited robustness for image data not seen by the neural network in the training phase[30]. Upsampling the input widefield image to 40 nm pixel size leads to a reasonable representation of image features with moderate improvement in resolution (142 ± 3 nm FRC resolution), upsampling to 65 nm pixel size leads to a largely inaccurate outcome, but with high precision, indicated by a large improvement in the overall FRC curve (123 ± 6 nm FRC resolution). Both settings lead to an anisotropic noise enhancement, larger in magnitude than for RL-deconvolution. Figure 5 and Supplementary Fig. 5 also show the result of denoising with a Hessian (H) regularization[31,32]. This method does indeed reduce the noise level for high spatial frequencies, but unfortunately at the expense of resolution (158.7 ± 0.1 nm FRC resolution) and a varying, anisotropic, noise variance in Fourier space.

Conclusion

In summary, we have proposed three new, complementary image reconstruction methods for SIM. They reduce or fully eliminate ad hoc user-adjustable reconstruction parameters. In general, it is

recommended to use the true-Wiener reconstruction as the default reconstruction, as this method seems to give the best overall compromise between contrast, resolution and noise profile. The noise fraction map can be used to quantitatively assess the noise enhancement artifact. Based on the examined datasets, we propose that noise enhancement can be characterized as severe, mild or nihil when associated with noise fraction ranges $Z_k > 0.4$, $0.4 \geq Z_k > 0.2$ and $0.2 \geq Z_k$, respectively. In the case of severe noise enhancement, it is recommended to either use the flat-noise (2D) or the notch-filtered (3D) reconstruction, specifically for image features on the intermediate length scale of around λ/NA, typically in the range 200–400 nm. As to further deconvolution, it seems that the RL method applied to (flat-noise) SIM gives the best overall performance in terms of simplicity, resolution and degree of noise enhancement.

These proposed reconstructions can also be used for SIM with a reduced number of acquired images[33], and also for other modalities. True-Wiener filtering can be directly generalized to widefield imaging, as well as image scanning and rescan microscopy approaches[6] and, with an analysis of noise propagation, be extended to lattice light sheet microscopy[34] and to tomographic imaging modalities[35]. In a next step in algorithm development, the regularization could be made to depend on spatial frequency as well as on the position in the imaged field[36], depending on the spectral and local

SNR. In-depth knowledge of noise and noise propagation in complex computational imaging techniques can also be used to steer or optimize different regularized approaches[31], as well as DL-based deconvolution, reconstruction or denoising[29,37–39] methods. Finally, the use of spectral SNR and the generation of image representations with a flat-noise spectrum open up objective methods to assess the relative benefits of any super-resolution or deconvolution method.

Online content

Any methods, additional references, Nature Research reporting summaries, source data, extended data, supplementary information, acknowledgements, peer review information; details of author contributions and competing interests; and statements of data and code availability are available at https://doi.org/10.1038/s41592-021-01167-7.

References

1. Neil, M. A. A., Juskaitis, R. & Wilson, T. Method of obtaining optical sectioning by using structured light in a conventional microscope. *Opt. Lett.* **22**, 1905–1907 (1997).
2. Heintzmann, R. & Cremer, C. Laterally modulated excitation microscopy: improvement of resolution by using a diffraction grating. *Proc. SPIE* **3568**, 185–196 (1999).
3. Gustafsson, M. G. L. Surpassing the lateral resolution limit by a factor of two using structured illumination microscopy. *J. Microsc.* **198**, 82–87 (2000).
4. Gustafsson, M. G. L. et al. Three-dimensional resolution doubling in wide-field fluorescence microscopy by structured illumination. *Biophys. J.* **94**, 4957–4970 (2008).
5. Schermelleh, L. et al. Subdiffraction multicolor imaging of the nuclear periphery with 3D structured illumination microscopy. *Science* **320**, 1332–1336 (2008).
6. Heintzmann, R. & Huser, T. Super-resolution structured illumination microscopy. *Chem. Rev.* **117**, 13890–13908 (2017).
7. Kner, P., Chhun, B. B., Griffis, E. R., Winoto, L. & Gustafsson, M. G. L. Super-resolution video microscopy of live cells by structured illumination. *Nat. Methods* **6**, 339–342 (2009).
8. Shao, L., Kner, P., Rego, E. H. & Gustafsson, M. G. L. Super-resolution 3D microscopy of live whole cells using structured illumination. *Nat. Methods* **12**, 1044–1046 (2011).
9. Fiolka, R., Shao, L., Rego, E. H., Davidson, M. W. & Gustafsson, M. G. L. Time-lapse two-color 3D imaging of live cells with doubled resolution using structured illumination. *Proc. Natl Acad. Sci. USA* **109**, 5311–5315 (2012).
10. Heintzmann, R., Jovin, T. & Cremer, C. Saturated patterned excitation microscopy – a concept for optical resolution improvement. *J. Opt. Soc. Am. B* **19**, 1599–1609 (2002).
11. Gustafsson, M. G. L. Nonlinear structured-illumination microscopy: wide-field fluorescence imaging with theoretically unlimited resolution. *Proc. Natl Acad. Sci. USA* **102**, 13081–13086 (2005).
12. Rego, E. H. et al. Nonlinear structured-illumination microscopy with a photoswitchable protein reveals cellular structures at 50-nm resolution. *Proc. Natl Acad. Sci. USA* **109**, E135–E143 (2012).
13. Li, D. et al. Extended-resolution structured illumination imaging of endocytic and cytoskeletal dynamics. *Science* **349**, aab3500 (2015).
14. Wicker, K., Mandula, O., Best, G., Fiolka, R. & Heintzmann, R. Phase optimization for structured illumination microscopy. *Opt. Express* **21**, 2032–2049 (2013).
15. Křížek, P., Lukeš, T., Ovesný, M., Fliegel, K. & Hagen, G. M. SIMToolbox: a MATLAB toolbox for structured illumination fluorescence microscopy. *Bioinformatics* **32**, 318–320 (2016).
16. Müller, M., Mönkemöller, V., Hennig, S., Hübner, W. & Huser, T. Open-source image reconstruction of super-resolution structured illumination microscopy data in ImageJ. *Nat. Commun.* **7**, 10980 (2016).
17. Ball, G. et al. SIMcheck: a toolbox for successful super-resolution SIM imaging. *Sci. Rep.* **5**, 15915 (2015).
18. Demmerle, J. et al. Strategic and practical guidelines for successful structured illumination microscopy. *Nat. Protoc.* **12**, 988–1010 (2017).
19. Sahl, S. J. et al. Comment on extended-resolution structured illumination imaging of endocytic and cytoskeletal dynamics. *Science* **352**, 527 (2016).
20. Li, D. et al. Response to comment on 'Extended-resolution structured illumination imaging of endocytic and cytoskeletal dynamics'. *Science* **352**, 527 (2016).
21. Righolt, C. H. et al. Image filtering in structured illumination microscopy using the Lukosz Bound. *Opt. Express* **21**, 24431–24451 (2013).
22. Fried, D. L. Noise in photo-emission current. *Appl. Opt.* **4**, 79–80 (1965).
23. Hu, S. et al. Structured illumination microscopy reveals focal adhesions are composed of linear subunits. *Cytoskeleton* **72**, 235–245 (2015).
24. Unser, M., Trus, B. L. & Steven, A. C. A new resolution criterion based on spectral signal-to-noise ratio. *Ultramicros* **23**, 39–52 (1987).
25. Nieuwenhuizen, R. P. J. et al. Measuring image resolution in optical nanoscopy. *Nat. Methods* **10**, 557–562 (2013).
26. Chakrova, N., Heintzmann, R., Rieger, B. & Stallinga, S. Studying different illumination patterns for resolution improvement in fluorescence microscopy. *Opt. Express* **23**, 31367–31383 (2015).
27. Heintzmann, R. Estimating missing information by maximum likelihood deconvolution. *Micron* **38**, 136–144 (2007).
28. Perez, V., Chang, B.-J. & Stelzer, E. H. K. Optimal 2D-SIM reconstruction by two filtering steps with Richardson–Lucy deconvolution. *Sci. Rep.* **6**, 37149 (2016).
29. Wang, H. et al. Deep learning enables cross-modality super-resolution in fluorescence microscopy. *Nat. Methods* **16**, 103–110 (2019).
30. Hoffman, D. P., Slavitt, I. & Fitzpatrick, C. A. The promise and peril of deep learning in microscopy. *Nat. Methods* **18**, 131–132 (2021).
31. Huang, X. et al. Fast, long-term, super-resolution imaging with Hessian structured illumination microscopy. *Nat. Biotechnol.* **36**, 451–459 (2018).
32. Markwirth, A. et al. Video-rate multi-color structured illumination microscopy with simultaneous real-time reconstruction. *Nat. Commun.* **10**, 4315 (2019).
33. Ströhl, F. & Kaminski, C. F. Speed limits of structured illumination microscopy. *Opt. Lett.* **42**, 2511–2514 (2017).
34. Chen, B.-C. et al. Lattice light-sheet microscopy: Imaging molecules to embryos at high spatiotemporal resolution. *Science* **346**, 1257998 (2014).
35. van der Horst, J., Trull, A. K. & Kalkman, J. Deep-tissue label-free quantitative optical tomography. *Optica* **7**, 1682–1689 (2020).
36. Boulanger, J., Pustelnik, N., Condat, L., Sengmanivong, L. & Piolot, T. Nonsmooth convex optimization for structured illumination microscopy image reconstruction. *Inverse Prob.* **34**, 095004 (2018).
37. Weigert, M. et al. Content-aware image restoration: pushing the limits of fluorescence microscopy. *Nat. Methods* **15**, 1090–1097 (2018).
38. Jin, L. et al. Deep learning enables structured illumination microscopy with low light levels and enhanced speed. *Nat. Commun.* **11**, 1934 (2020).
39. Krull, A. et al. Noise2Void—learning denoising from single noisy images. in *Proc. 2019 IEEE/CVF Conference on Computer Vision and Pattern Recognition (CVPR)* 2124–2132 (IEEE, 2019).

Methods

Microscope setups. Images for Figs. 1–3 and 5 and Extended Data Figs. 1, 2, 4 and 5 were acquired with a commercial Zeiss Elyra PS1 system, using a ×63/1.40 oil immersion objective and a 1004×1002, 8 μm pixel, Andor iXon3 885 EM-CCD camera. A magnification-adapted tube lens is used giving rise to a 79 nm backprojected pixel size. Raw images are acquired for five rotations and five translations of the line illumination pattern.

Images for Fig. 4 and Extended Data Figs. 6–10 were acquired with a commercial DeltaVision OMX V3 Blaze (GE Healthcare) instrument, using a ×60/1.42 PlanApo oil immersion objective (Olympus) and a 2048×2048, 6.5 μm pixel, PCO edge 4.2 sCMOS cameras with a magnification-adapted tube lens giving rise to a 82 nm backprojected pixel size. Raw images are acquired for three rotations and five translations of the line illumination pattern.

The raw images used for the reconstructions shown in Extended Data Fig. 3 are recorded with a DMD-SIM setup described in detail elsewhere[26]. In short, multispot arrays with a pitch of ten DMD-pixels (DMD-pixel size 13.68 μm) were created using 488-nm despeckled laser illumination and projected onto the sample via a relay path and a ×60/0.7 air objective (projected DMD-pixel size 137 nm) of an Olympus IX71 microscope and subsequently scanned across the sample. The images were captured on a 2048×2048, 6.5 μm pixel, Hamamatsu Orca Flash 4.0 camera (projected pixel size 108 nm).

Samples. Figures 1, 2 and 5, Extended Data Fig. 1 and Supplementary Fig. 5 show data of GFP-zyxin expressing U2OS cells. Zyxin is an integral protein in focal adhesions, protein complexes that form a connection between the extracellular matrix through integrin receptors and the actin cytoskeleton, through its interaction with α-actinin[40] and the stretch sensitive protein p130[cas] in which it acts as one of the mechanosensing components in focal adhesions[41,42]. Sterile high precision coverslips #1.5H (Marienfeld Superior) were incubated with 10 μg/ml purecol (Advanced Biomatrix) overnight at 4 °C and subsequently washed three times with PBS. U2OS cells were grown in DMEM medium and transfected with GFP-zyxin (a gift from J. de Rooij). The cells were fixed for 20 min in 4% formaldehyde/PBS buffer and mounted on a glass slide in Vectashield antifade mounting medium (Vector Laboratories). Cells grown on collagen-coated coverslips typically show rod-shaped focal adhesions, consisting of parallel linear structures[23]. Zyxin is also observed to be present on actin fibers in distinct patches.

Figure 3 and Extended Data Fig. 4 show data of nanofabricated fluorescent test structures patterned using a previously published method[43], that was slightly adopted for higher resolution patterning. In short, a monolayer of 3-[methoxy(polyethyleneoxy)propyl]trimethoxysilane (ABCR) was covalently grafted onto ITO-coated no.1 cover glass (Optics Balzers) and exposed locally to a focused electron beam following the defined patterns. After removal from the scanning electron microscope, the sample was incubated for 45 min with a 100 nM IgG-Alexa Fluor 488 solution in 1× TE buffer. Samples were then washed with TE buffer and deionized water, followed by drying and transfer to the optical microscope.

Extended Data Fig. 5 shows data of the mCherry-SYCP3 protein in the synaptonemal complex. Mouse oocytes from mice expressing mCherry-SYCP3[44] were isolated and spread[45] on #1.5H high precision coverslips and embedded in prolong gold (Invitrogen). SYCP3 is part of the lateral element of the synaptonemal complex that is formed during meiosis prophase I. The synaptonemal complex is comprised of two lateral elements that form parallel linear protein assemblies at a distance of ~220 nm apart[46].

Figure 4, Extended Data Fig. 6 and Supplementary Videos 3–6 show data collected from 4%-formaldehyde-fixed mouse C127 cells grown on #1.5H high precision coverslips, immunostained for microtubules using DM1A mouse monoclonal anti-α-tubulin primary antibodies (Sigma-Aldrich) and donkey anti-mouse Alexa Fluor 488 secondary antibodies (Thermo Fisher) and mounted in Vectashield H-1000 medium (Vector Laboratories). Extended Data Fig. 7 shows data of a monolayer of 100 nm yellow–green FluoSphere beads (Thermo Fisher), dried and mounted in glycerol[18]. Extended Data Fig. 9 and Supplementary Video 8 show data of a 2%-formaldehyde-fixed C127 cell immunolabeled with rabbit anti-histone H3K4me3 primary antibodies (Active Motif) and goat-anti-rabbit Alexa Fluor 488 secondary antibodies (Thermo Fisher), counterstained with 4,6-diamidino-2-phenylindole (DAPI) and mounted in Vectashield. Supplementary Video 9 and Extended Data Fig. 10 show live cell data of stably expressing histone H2B-GFP grown in a 35 mm μ-Dish with high precision glass bottom (Ibidi) and imaged at 37 °C and 5% CO₂. A time series was recorded with 2 s intervals. For each time point, seven z-sections with z-distance of 0.125 μm were acquired (in total 7×3×5 = 105 raw images per time point).

Extended Data Figs. 2, 3 and 8 and Supplementary Video 7 show data of a bovine pulmonary artery endothelial cell (BPAEC), with mitochondria labeled with MitoTracker Red, actin labeled with Alexa Fluor 488 and DNA labeled with DAPI and embedded in hardening mounting medium (Thermo Fisher Fluo Cells slide no. 1).

SIM processing and reconstruction. The data shown in Figs. 1–3 and 5 and Extended Data Figs. 1, 2, 4 and 5 pertain to 2D-SIM reconstructions made from a single focal slice of a 3D-SIM acquisition, that is, made with a three-beam

interference illumination pattern. The data shown in Fig. 4 and Extended Data Figs. 6–10 pertain to full 3D-SIM reconstructions. A flow diagram illustrating the different steps in making (2D and 3D) SIM reconstructions is shown in Supplementary Fig. 6, and consists of preprocessing steps, illumination pattern estimation and image Fourier order computation steps, and filtering and reconstruction operations.

Preprocessing steps. The set of preprocessing operations starts with a gain and offset calibration for providing image signals that represent the number of detected photoelectrons[47]. The EM-CCD or sCMOS cameras that are used have zero or negligible readout noise so that the image signals follow Poisson statistics to a good approximation. Some effects of fixed pattern noise (pixel-to-pixel variations in offset and gain) are visible in sCMOS based images, but are ignored here for the sake of simplicity. In a future study, this could possibly be incorporated by a further camera calibration step, or by extending the method of Heintzmann et al.[47]. Optionally, the images are grouped in sets of five images acquired with the same illumination pattern angle, and registered in an all-to-one manner to correct for drift. It turns out that leaving out the step of drift correction does not substantially deteriorate the reconstruction outcomes for the imaged specimens.

The illumination pattern modulation in 3D-SIM can be characterized by the modulation contrast to noise ratio (MCNR), a quality measure for faithful illumination pattern retrieval that is part of the SIMcheck quality control software package[17]. The proposed method of computation of the MCNR (ref. [17]) involves images acquired at different focal planes, and can therefore not be applied directly to 2D-SIM. To that end, we used an alternative way to compute the MCNR that can be computed per pixel/voxel. Starting point is a one-dimensional FT of the five-phase step images for each pixel/voxel to the set of photon counts N_j of each pixel (voxel) for the phase steps $j = 1, 2, …, M_t$, resulting in the fit:

$$N_j = A_0 + A_1 \cos\left(\frac{2\pi j}{M_t} + \varphi_1\right) + A_2 \cos\left(\frac{4\pi j}{M_t} + \varphi_2\right) \qquad (7)$$

The modulation is taken as twice the root-squared average of the first and second-order Fourier coefficients A_1 and A_2, and the shot noise level is the square root of the zeroth Fourier coefficient A_0. This leads to:

$$\text{MCNR} = \frac{2\sqrt{A_1^2 + A_2^2}}{\sqrt{A_0}} \qquad (8)$$

The results obtained with the current proposal for computing the MCNR agree well with the results obtained with SIMcheck, although there are small quantitative differences. For example, the lack of averaging Fourier coefficients over focal slices gives a more noisy appearance of the MCNR across the field of view for low signal acquisitions. The rule-of-thumb for reliable pattern parameter estimation is to have sufficient foreground pixels/voxels with MCNR ≥ 3. The MCNR is actually a SIM reconstruction in itself, which generalizes the original SIM proposal[1] by including the second-order Fourier coefficients, and shows some degree of optical sectioning (Supplementary Fig. 1). The peak MCNR averaged over the pattern orientations per focal slice has a maximum as a function of the focal slice (Supplementary Fig. 7). Having a satisfactory MCNR only for a limited range of focus positions may be attributed to not just a limited axial extent of the sample, but also to spherical aberration caused by refractive index mismatch. For typical high-NA immersion microscopes, the refractive index of the immersion medium must be controlled at the 10^{-3} level for optimum results[18], and the axial range of images with useful modulation seems to be typically only a few micrometers. For 2D-SIM processing, we take the focal slice with the maximum illumination pattern modulation.

So-called z-wrapping artifacts[18] may arise for datasets with a limited number of focal slices, as, for example, many live cell 3D datasets. The periodic boundary conditions of the FT then perturb the first and final few of the slices of the reconstruction. This can be mitigated by preferably ignoring these, or by representing only the final SIM reconstruction by a maximum intensity projection of the reconstruction stack. Another method to mitigate the effect of z-wrapping artifacts is by adding several extra, fictitious, focus layers. The reconstructions for the live cell dataset of Supplementary Video 9 and Extended Data Fig. 10, which is based on just seven focal slices, are made using 14 extra layers. It is estimated that the required number of extra layers is in the range of 10–20. These extra focus layers interpolate linearly between the first and last slice of the focus stack. Further, they are blurred by convolution with a Gaussian kernel to mimic the effect of defocus. The kernel size ranges from one pixel for the layers directly adjacent to the first and last focal slice, to 20 pixels for the layer(s) in the middle of the fictitious extra stack. Finally, artificial shot noise is added for maintaining Poisson statistics.

The next step in preprocessing is to apply a window to the data cube to enforce continuity in the periodic boundary conditions assumed in subsequent FTs, that is, for eliminating streaking along the coordinate axes in the FTs. For the voxel indices $j = 1, …, N$ along any of the three coordinate axes we can define a scaled coordinate $r_j = (2j - 1 - N) / (2N)$, the windowing is applied to the edges defined by $1/2 - |r_j| \leq b$, where we take b in the range 0.1–0.2 along the lateral directions

($r=x$ and $r=y$) and $b=0$ along the axial direction ($r=z$). Over these boundary region voxels, the window function is taken to be $\tau_j = \sin\left(\pi\left(1 - 2\left|r_j\right|\right)/(4b)\right)^2$, for the inner voxels $\tau_j = 1$ is taken. The overall window function is the product of the window functions for the three orthogonal coordinate axes. No windowing is applied in the axial direction because it seems to have limited use there. The first and last focal slice typically show no recognizable structure as all object features are drowned by defocus and spherical-aberration-induced loss of illumination pattern modulation, which implies that the discontinuity arising from the FT periodic boundary conditions in the axial direction is not that harmful. The further fictitious layers that interpolate between the first and last focal slice, with features that are gradually blurred away, play the same role for datasets with limited number of focal slices. A further factor here is that the axial Fourier streak is suppressed anyway by the low-pass filtering step with the 3D-OTF of the microscope, which has the well-known missing cone.

By a simple pointwise multiplication of the image data cube with the window function, the windowing operation compromises Poisson statistics of the image signals. This can be overcome by applying the random binomial data splitting approach (Supplementary Note 2). The image signal for a pixel is written as $I = n + \varepsilon$, where $n = \text{round}(I)$. The value of the window function for this pixel τ satisfies $0 \leq \tau \leq 1$ and is used as the probability in a binomial probability distribution for each of the integer n photon counts, giving a random total of n' counts satisfying $0 \leq n' \leq n$. The remainder ε is reduced by the ratio n'/n. This procedure preserves Poisson statistics across the entire data cube.

The next preprocessing step is upsampling to accommodate the extended cutoff of the SIM OTF (typically by a factor of two in the lateral directions, no upsampling in the axial direction) by zero padding in Fourier space. This operation compromises Poisson statistics, but this can be solved by artificially filling the extra high spatial-frequency Fourier pixels, which are created by zero padding, with noise. For each voxel in the upsampled image with upsampled image signal n, a random variable n' is generated using the signal n as Poisson rate. The difference $n' - n$, the artificially created noise, is Fourier transformed and masked to fill the new Fourier pixels created by zero padding, while keeping the original Fourier pixels obtained from the FT of n unaltered. Inverse FT then gives an upsampled image that follows Poisson statistics.

Illumination pattern parameters and OTF. The illumination pattern parameters (pitch, orientation and phases) are estimated using a 2D-projection of the preprocessed 3D dataset. This projection is the (weighted) sum over all focal slices, where the average MCNR values over each focal slice is taken as weight. This improves SNR by averaging over noise in the individual images and over the 3D-structure of the fluorescent object, but under the assumption that these gains are bigger than possible residual shifts in the illumination patterns between different focal slices, left after possible drift correction. Next, the cross-correlation image matrix for all $M_t \times M_t$ image combinations with different pattern phases is computed, zoomed in at regions around integer multiples of the expected Fourier peaks at $\mathbf{q}_{\text{est}}$. The peak in the root-mean square of the cross-correlation matrix is used to update the estimate of the pattern spatial-frequency vector $\mathbf{q}_{\text{est}}$ (see Supplementary Note 1 for more detail). The precision of peak detection is aided by the zooming capability of the chirp z-transform for evaluating FTs[48], reaching a relative precision in determining the pitch equal to 6×10^{-5} over the $K = 10$ noise-independent acquisitions of the GFP-zyxin dataset and 8×10^{-5} over the 15 frames of the live cell histone H2B-GFP dataset. The pattern phases are estimated from the phase of the autocorrelation peaks[49], reaching a precision of around 1 deg for the GFP-zyxin and for the live cell histone H2B-GFP datasets.

The retrieved values for the pitch, orientations, and phases of the illumination patterns are used to compute the different image Fourier orders (zeroth, first and second) per orientation of the line illumination pattern, and to shift these orders in the lateral direction to the correct location in Fourier space.

The 3D-OTF is obtained from a bead calibration experiment[18], if such data are available. The illumination pattern parameters are used to create laterally shifted copies of the different Fourier orders per orientation of the line illumination pattern. An alternative to the calibration OTF is computation using a vectorial point spread function (PSF) model, taking all effects of high NA and polarization into account (see, for example, ref. [50] and references therein). For 3D datasets, this requires further axial separation of the two branches of the first Fourier order. The theoretical value $k_z = \pm n_{\text{med}}\left(1 - \cos\theta\right)/\lambda_{\text{ex}}$ is used, with λ_{ex} the excitation wavelength, n_{med} the medium refractive index and $\sin\theta = \lambda_{\text{ex}}/(n_{\text{med}}p)$, where p is the estimated illumination pattern pitch.

Finally, the first- and second-order strengths a_1 and a_2 are estimated from the image data itself by requiring consistency across order overlap regions, as the different orders depend on the spatial-frequency spectrum of the same underlying fluorescent object (see Supplementary Note 1 for more detail). It turns out that the retrieved order strengths depend on the signal-to-noise ratio and sparsity of the sample, leading to lower estimates for relatively dense samples and/or samples recorded under adverse signal-to-noise conditions. The estimated order strengths should therefore be seen as effective order strengths, not as the true underlying values. A fixed set of order strengths in the range of values found for the sparse tubulin set of Fig. 4 measured at high signal levels ($a_1 = 0.30$ and $a_2 = 0.45$) is used for all SIM reconstructions.

Reconstruction. The functions $\hat{D}_j$ and $\hat{V}_j$ (defined in Supplementary Note 2) are computed from copies of the incoherent (2D or 3D) OTF, shifted in Fourier space, and from the order strengths a_1 and a_2. This is sufficient to obtain the regularization filter for flat-noise SIM. For state-of-the-art and true-Wiener SIM we use as apodization filter the trianglex filter $\hat{A}_j = \hat{\Lambda}_j^x$ with $\hat{\Lambda}_j$ the triangular filter (interpolating linearly between 1 at zero spatial frequency to 0 at the extended SIM cutoff) and $x = 0.4$ a numerical coefficient, because this has also been used in the literature[13,14]. The triangular filter with $x = 1$ gives a reconstruction visually similar to that of the Lukosz-bound filter[21], and is more benign for artifacts, such as the structured noise artifact and the z-wrapping artifact that arises for low number of focal slices, than the trianglex filter with $x = 0.4$.

An initial pre-Wiener-filtered SIM reconstruction is made by low-pass filtering the different image Fourier orders with the corresponding shifted copy of the incoherent OTF, and then adding all contributions weighted with order strengths. Overall Wiener filters $\hat{A}_j/\left(\hat{D}_j + w\right)$ and $1/\left(\hat{D}_j + \hat{w}_j\right) = 1/\sqrt{\hat{V}_j}$ are applied and a subsequent inverse FT is executed to generate state-of-the-art and flat-noise SIM reconstructions, respectively.

The pre-Wiener-filtered SIM reconstruction is used to make an estimate of the SSNR needed for the true-Wiener-filtered SIM reconstruction. The initial SIM reconstruction $e_k^{\text{rec},i}$ has a spectral power $\left|\hat{e}_j^{\text{rec},i}\right|^2 = \left|\hat{e}_k^i + \delta\hat{e}_k^i\right|^2 = \left|\hat{e}_k^i\right|^2 + 2\text{Re}\left\{\hat{e}_k^{i*}\,\delta\hat{e}_k^i\right\} + \left|\delta\hat{e}_k^i\right|^2$. Averaging over rings in spatial-frequency space effectively eliminates the signal-noise cross-term. The average $\left\langle \hat{N}_j^i \right\rangle_{\text{ring}}$ of the noise power $\left|\delta\hat{e}_k^i\right|^2$ is independent of the object spectrum and is proportional to the noise variance function (equation (2)). The estimate for the SSNR is then found as:

$$\text{SSNR}_j \approx \frac{\left\langle \left|\hat{e}_j^{\text{rec},i}\right|^2\right\rangle_{\text{ring}}}{\left\langle \hat{N}_j^i \right\rangle_{\text{ring}}} - 1 \tag{9}$$

which can subsequently be used with equation (5) to find the regularization filter for the final true-Wiener-filtered reconstruction. A minor drawback of ring averaging is that azimuthal variations in SSNR are not accounted for. Averaging schemes based on for example Gaussian blurring over regions in spatial-frequency space can possibly provide an alternative in case these azimuthal variations become relevant.

The error in the estimated SSNR becomes comparable with the SSNR for the highest spatial frequencies, where there is too little signal (for example, Fig. 1m). This issue can be solved by extrapolating the regularization filter from low spatial frequencies to high spatial frequencies. The simplest extrapolation is to take the maximum of $\hat{w}(\mathbf{q})$ for spatial frequencies in the region $\langle\text{SSNR}(\mathbf{q})\rangle_{\text{ring}} > \text{SSNR}_{\text{thr}}$ and use this as a constant regularization in the region $\langle\text{SSNR}(\mathbf{q})\rangle_{\text{ring}} < \text{SSNR}_{\text{thr}}$. Here SSNR_{thr} is a threshold value that can typically be selected from the range between about 1 and 10. A bit more complex is a quadratic extrapolation $\hat{w}(\mathbf{q}) = \alpha \left|\mathbf{q}\right|^2$, where the parameter α is estimated from the spatial-frequency region defined by $\langle\text{SSNR}(\bar{q})\rangle_{\text{ring}} > \text{SSNR}_{\text{thr}}$. This corresponds to a regularization function in real space $\alpha \left|\nabla e\right|^2$, with ∇ the 2D- or 3D-gradient operator[21]. A more general power–law extrapolation $\hat{w}(\mathbf{q}) = \alpha \left|\mathbf{q}\right|^\beta$ works fine in many cases as well, where now both parameters α and β are estimated from the spatial-frequency region defined by $\langle\text{SSNR}(\bar{q})\rangle_{\text{ring}} > \text{SSNR}_{\text{thr}}$. Typical values found for the power–law exponent β are in the range $1.2 < \beta < 2.7$. For the sake of simplicity, we have used the quadratic extrapolation scheme with $\text{SSNR}_{\text{thr}} = 5$ for all datasets.

Notch filtering of the different image Fourier orders has been applied to improve the optical sectioning in SIM, mostly for 2D-SIM reconstructions[14,16]. The retrieved orders (before lateral shifting in Fourier space) are multiplied with filter kernels as defined in equations (3.21), (3.22) and (3.23) in Supplementary Note 3. The notch depths α_0, α_1 and α_2, the lateral notch width $\Delta q_\parallel$ and, for 3D-SIM, the axial notch width $\Delta q_\perp$, arising in the filters are in principle user-adjustable parameters. Instead of an ad hoc choice, we fix the parameter values to optimize the contrast of flat-noise SIM by making the flat-noise OTF $\hat{g}_j^{\text{FN-SIM}} = \hat{D}_j/\sqrt{\hat{V}_j}$ as close as possible to a target OTF, which we take to be equal to the Lukosz-bound apodization function. A suitable OTF error function for this optimization is defined in equation (3.26) in Supplementary Note 3. Reasonably good results can be obtained for notch widths that scale with the cutoff frequency $\Delta q_\parallel = 2\rho\text{NA}/\lambda_{\text{ex}}$, and, for 3D-SIM $\Delta q_\perp = \rho\left(n_{\text{med}} - \sqrt{n_{\text{med}}^2 - \text{NA}^2}\right)/\lambda_{\text{ex}}$, where we take the numerical prefactor $\rho = 1.25$. For 2D-SIM, it is sufficient to apply the notch filtering to the zeroth order only, that is $\alpha_1 = \alpha_2 = 0$. The remaining nonzero notch depth $\alpha_0 = 1 - 10^{-d_0}$ is determined using MATLAB's fminbnd to find the optimum value of the notch dip exponent d_0. The procedure converges in about ten iterations with a precision of around 10^{-3}. Typically this results in values in the range $1.5 \leq d_0 \leq 3$. The final notch-filtered images do not depend hugely on the initial choice for the parameter ρ, generally a value $\rho > 0.75$ will suffice, but small differences can arise between different datasets. The task of optimizing the flat-noise OTF is more complex for 3D-SIM, because the requirement on the axial transfer function comes on top of the requirement on the lateral transfer function, and because the native flat-noise OTF has rather pronounced peaks at the center spatial frequencies of the contributing orders. It turns out that applying a notch

filter to all contributing orders is now necessary, especially as this seems beneficial for diminishing the susceptibility for hexagonal background imprint artifacts. For the sake of simplicity, we take $\alpha_0 = \alpha_1 = \alpha_2 = 1 - 10^{-d_n}$, and again use MATLAB's fminbnd to find the optimum value of the notch dip exponent d_n. Typically, this results in values in the range $3.5 \leq d_n \leq 5.5$. It is quite conceivable that more sophisticated designs for the (notch) filters could improve the current results.

Noise assessment. The noise model is validated by the spectral noise variance and SSNR that are obtained from the $K = 10$ noise-independent acquisitions of the GFP-zyxin dataset by computing the unbiased sample variance over the K reconstructions. The spectral noise variance for the widefield reconstruction obtained by summing over the M_r rotations and M_t translations seems to be constant across the spatial-frequency spectrum with variations up to several percent (Fig. 1i). The small peak at low spatial frequencies is attributed to residual effects of photobleaching, illumination variations and drift. This small peak gives rise to satellite peaks in the experimental spectral noise variance for the SIM reconstructions at the center spatial frequencies of the orders that do not correspond to actual noise enhancement. FRC curves are computed[25] for all $K(K-1)/2$ pairs of reconstructions, the mean and s.d. over all these reconstruction pairs are plotted in all FRC results. FRC curves need no bleaching correction, as they are independent of overall intensity variations of the two input images. The model-independent noise assessment via the random binomial data splitting method is described in Supplementary Note 2.

Noise fraction map. The noise model enables the assessment of the fraction Z_k of the SIM reconstruction that is due to noise, based on the average signal and noise level in a neighborhood around each pixel k (Supplementary Note 2). We have implemented computation of this noise fraction by Gaussian smoothing with a width $\lambda/2NA$, which corresponds to about four SIM pixels. For smaller kernel sizes, there is insufficient noise averaging, for larger kernel sizes the noise fraction values of the background and of the foreground features is blurred too much. It is expected that $0 \leq Z_k \leq 1$, but values >1 can arise due to incomplete averaging of noise in the pixel neighborhood.

Deconvolution and denoising. Starting point for the 2D RL-deconvolution is a gain recalibration by fitting a straight line through the mean versus variance curve obtained from the K noise-independent reconstructions. This corrects for any possible changes to intensity level during the reconstruction and so ensures the best approximation to Poisson statistics for the signal at each pixel. The reason for this step is that RL-deconvolution can be framed as an object retrieval procedure, based on maximizing a likelihood function that is determined by Poisson statistics[27]. Suitable initial estimates of the nonlinear iterative algorithm are either the recorded widefield image (RL-widefield) or the flat-noise SIM reconstruction (RL-SIM). The OTF used in the RL-deconvolution algorithm is either the incoherent OTF (RL-widefield) or the flat-noise SIM OTF (RL-SIM). The iterative procedure is stopped when the error $\left(\sum_k \left(e_k^{n+1} - e_k^n\right)^2\right) / \left(\sum_k \left(e_k^n\right)^2\right)$, with e_k^n the nth estimate, is less than 10^{-5}. The resulting RL-SIM deconvolution has been compared to the joint RL-deconvolution[51,52] for this dataset, which gave visually the same outcome. For that reason, joint RL results are not shown.

The publicly available code for DL-based deconvolution[29] has been applied with no modification to upsampled widefield representations. The upsampling was performed by zero padding in Fourier space and subsequent filling the added zeros with noise components, just as done for the SIM preprocessing. The publicly available code for Hessian SIM[31] is applied in the denoise mode with the recommended parameter settings.

Image data visualization. All images are rendered with full dynamic range, that is, with no clipping whatsoever. The 3D live cell dataset of histone H2B-GFP is represented in Supplementary Video 9 by a maximum intensity projection, in view of the limited number (seven) of focal slices.

Reporting Summary. Further information on the research design is available in the Nature Research Reporting Summary linked to this article.

Data availability
Data are available at https://doi.org/10.4121/12942932.

Code availability
MATLAB code is available at https://github.com/qnano/simnoise. ImageJ code for 2D-SIM is available at https://github.com/fairSIM.

References
40. Reinhard, M. et al. An alpha-actinin binding site of zyxin is essential for subcellular zyxin localization and alpha-actinin recruitment. *J. Biol. Chem.* **274**, 13410–13418 (1999).
41. Suresh Babu, S. et al. Mechanism of stretch-induced activation of the mechanotransducer zyxin in vascular cells. *Sci. Signal.* **5**, ra91 (2012).
42. Yoshigi, M., Hoffman, L. M., Jensen, C. C., Yost, H. J. & Beckerle, M. C. Mechanical force mobilizes zyxin from focal adhesions to actin filaments and regulates cytoskeletal reinforcement. *J. Cell Biol.* **171**, 209–215 (2005).
43. Schlapak, R. et al. Painting with biomolecules at the nanoscale: biofunctionalization with tunable surface densities. *Nano Lett.* **12**, 1983–1989 (2012).
44. Enguita-Marruedo, A. et al. Live cell analyses of synaptonemal complex dynamics and chromosome movements in cultured mouse testis tubules and embryonic ovaries. *Chromosoma* **127**, 341–359 (2018).
45. Peters, A. H., Plug, A. W., van Vugt, M. J. & de Boer, P. A drying-down technique for the spreading of mammalian meiocytes from the male and female germline. *Chromosome Res.* **5**, 66–68 (1997).
46. Schücker, K., Holm, T., Franke, C., Sauer, M. & Benavente, R. Elucidation of synaptonemal complex organization by super-resolution imaging with isotropic resolution. *Proc. Natl Acad. Sci. USA* **112**, 2029–2033 (2015).
47. Heintzmann, R. et al. Calibrating photon counts from a single image. Preprint at https://arxiv.org/abs/1611.056541611.05654 (2016).
48. Bakx, J. L. Efficient computation of optical disk readout by use of the chirp z transform. *Appl. Opt.* **41**, 4897–4903 (2002).
49. Wicker, K. Non-iterative determination of pattern phase in structured illumination microscopy using autocorrelations in Fourier space. *Opt. Express* **21**, 24692–24701 (2013).
50. Stallinga & Rieger, B. Accuracy of the Gaussian Point Spread Function model in 2D localization microscopy. *Opt. Express* **18**, 24461–24476 (2010).
51. Ingaramo, M. et al. Richardson–Lucy deconvolution as a general tool for combining images with complementary strengths. *ChemPhysChem* **15**, 794–800 (2014).
52. Ströhl, F. & Kaminski, C. F. A joint Richardson–Lucy deconvolution algorithm for the reconstruction of multifocal structured illumination microscopy data. *Methods Appl. Fluoresc.* **3**, 014002 (2015).

Author contributions
Imaging experiments were done by C.S.S., J.A.S., L.S., N.C., W.v.C. and A.B.H. J.A.S., S.H., Y.V., C.W.H. and J.P.H. designed and manufactured nanofabricated test samples. C.S.S., N.C., M.M. and S.S. analyzed data. S.S. derived theory, wrote the paper and supervised the research. All authors read and approved the manuscript.

Competing interests
The authors declare no competing financial interests.
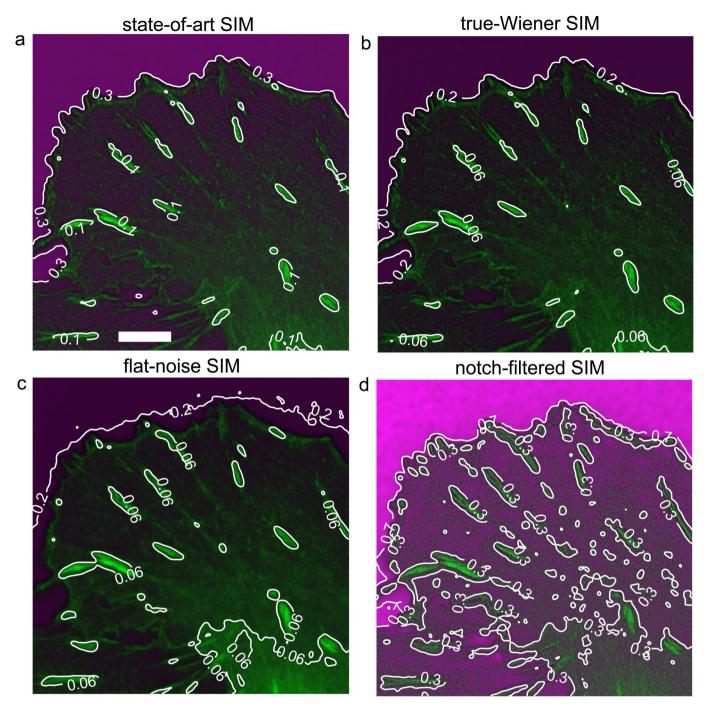
Additional information
Extended data is available for this paper at https://doi.org/10.1038/s41592-021-01167-7.

Supplementary information The online version contains supplementary material available at https://doi.org/10.1038/s41592-021-01167-7.
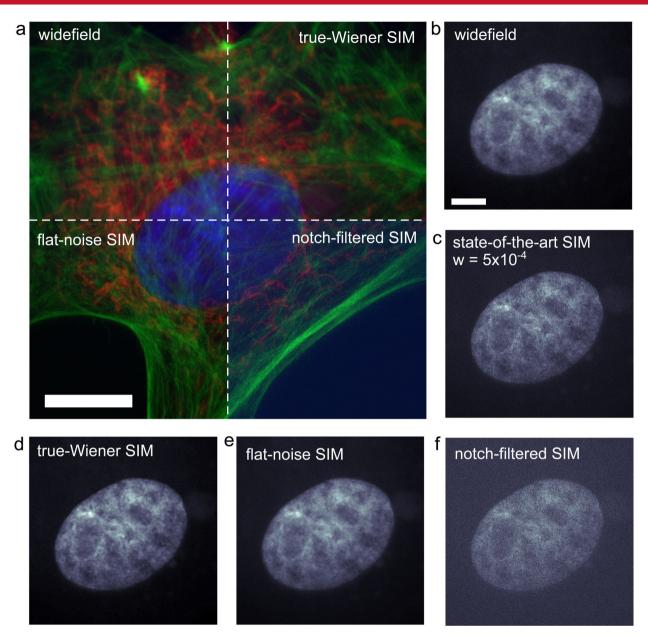
Correspondence and requests for materials should be addressed to S.S.

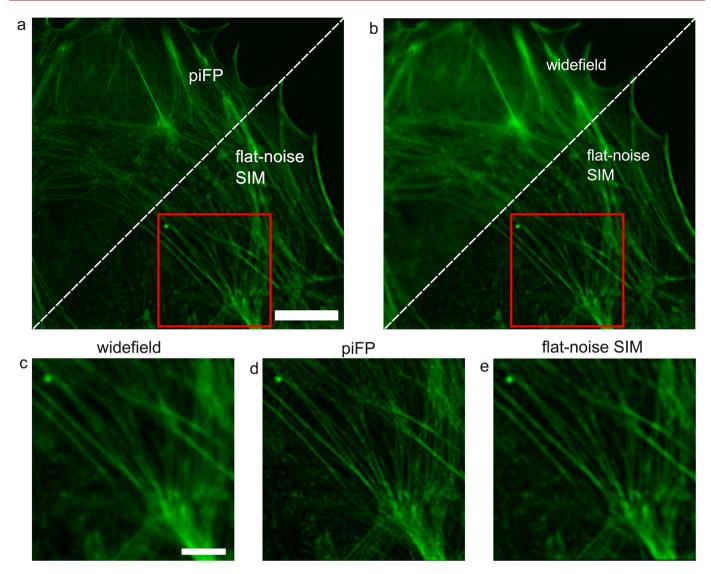**Reprints and permissions information** is available at www.nature.com/reprints.

Peer review Information *Nature Methods* thanks Florian Ströhl and the other, anonymous, reviewer(s) for their contribution to the peer review of this work. Rita Strack was the primary editor on this article and managed its editorial process and peer review in collaboration with the rest of the editorial team.
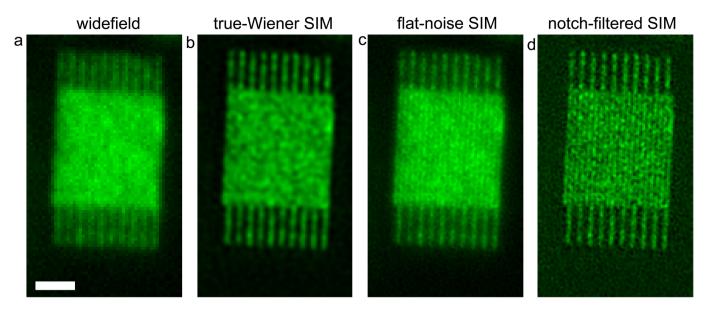
Extended Data Fig. 1 | Noise-controlled SIM reconstructions of GFP-zyxin protein in focal adhesions (green) and noise fraction map (magenta) over full FOV. a–d, State-of-art SIM ($w = 5 \times 10^{-4}$), true-Wiener SIM, flat-noise SIM, and notch-filtered SIM reconstructions. Contours of the noise fraction map are added in white with contour level indicated. In all reconstructions the noise fraction is lowest in the foreground features and highest in the background region outside the cell. Overall, flat-noise SIM and true-Wiener SIM offer the lowest, and notch-filtered SIM the highest noise enhancement. Scale bar 5 μm.
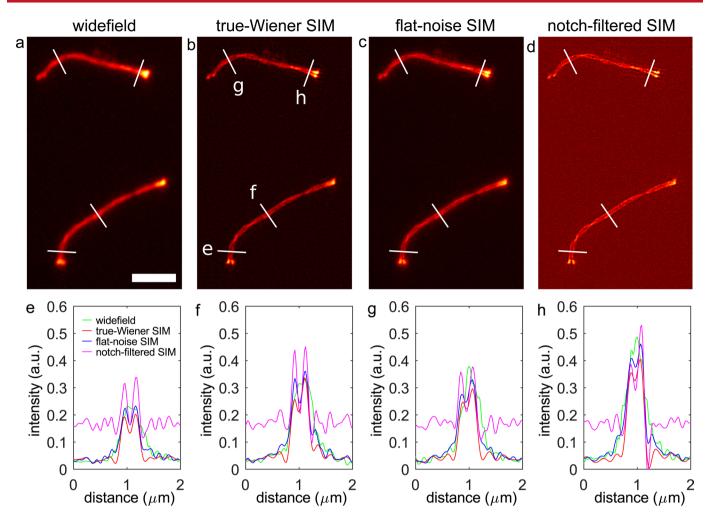
Extended Data Fig. 2 | Multi-color noise-controlled 2D-SIM reconstructions. a, Combined widefield, true-Wiener SIM, flat-noise SIM, and notch-filtered SIM reconstructions of a fluorescent test slide of a bovine pulmonary artery endothelial cell (red channel: mitochondria labeled with MitoTracker Red, green channel: actin labeled with Alexa Fluor 488, blue channel: DNA labeled with DAPI). Note that due to embedding in hardening mounting medium, cells are flattened and 3D nuclear morphology is compromised. **b-f**, Insets of the DAPI channel comparing state-of-the-art SIM with clear noise amplification artifact to the noise-controlled SIM reconstructions. The SSNR in the DAPI channel is low in this example case, due to reduced signal intensity and compromised morphology. The low SSNR is properly taken into account by the noise-controlled SIM reconstructions, without introducing artifacts, but not by the state-of-the-art SIM reconstruction. Scale bar (**a**) 10 µm, scale bar (**b-f**) 5 µm.
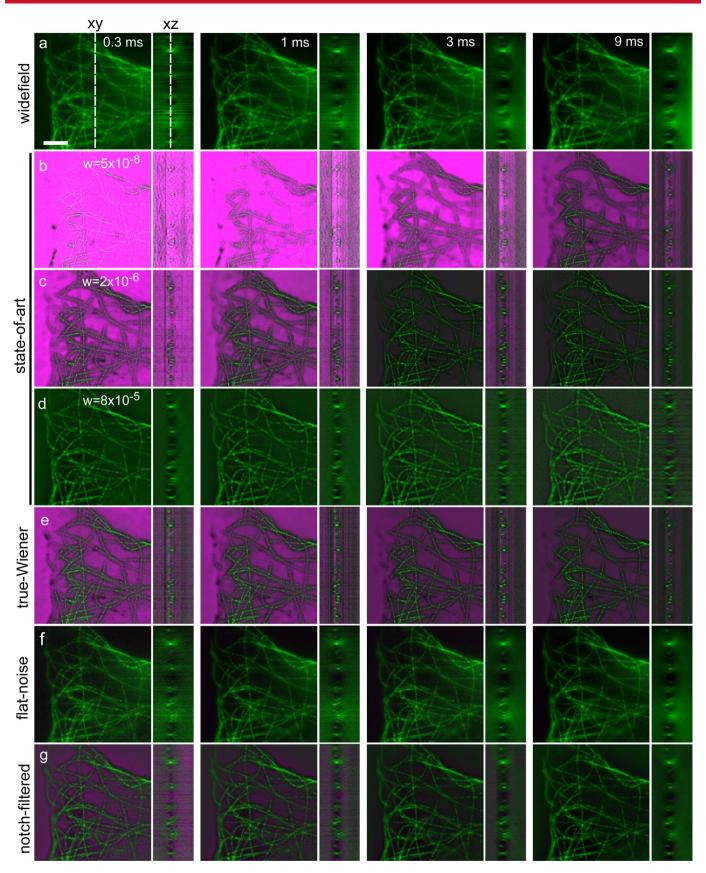
Extended Data Fig. 3 | Noise propagation in DMD-SIM. a, Reconstructions of Alexa Fluor 488 labeled actin filaments in a bovine pulmonary artery endothelial cell with the iterative pattern-illuminated Fourier Ptychography (piFP) algorithm (see Supplementary Note 1) and with a band-pass regularization approach for flat-noise SIM. **b**, Comparison of flat-noise SIM to a widefield reconstruction obtained by summing the whole set of acquired images. **c-e**, Insets of the boxed region in (**a**) and (**b**). Both piFP and flat-noise SIM offer a resolution improvement, but piFP has better contrast than flat-noise SIM. The piFP reconstruction shows corrugated line structures and punctuated features (upper right of insets), similar to the structured noise artifact in state-of-the-art SIM with line illumination patterns, flat-noise SIM shows this to a lesser degree. Scale bar (**a,b**) 10 μm, scale bar (**c-e**) 4 μm.
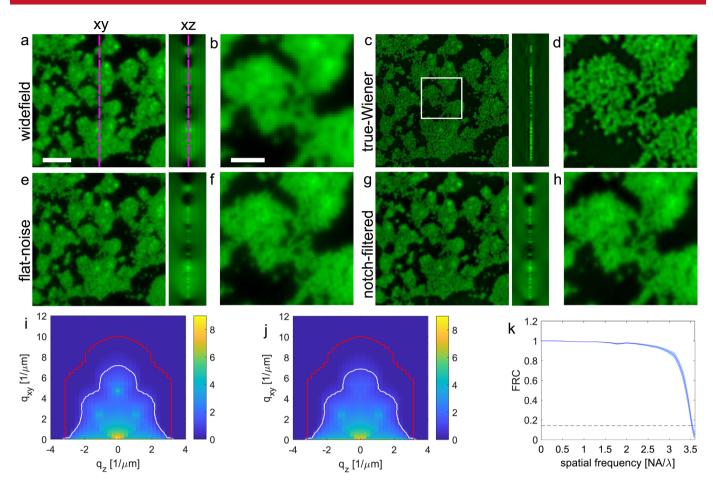
| widefield | true-Wiener SIM | flat-noise SIM | notch-filtered SIM |

Extended Data Fig. 4 | Flat-noise SIM provides better visibility of high spatial frequency structures. a–d, Widefield, true-Wiener, flat-noise, and notch-filtered SIM reconstructions of a nanofabricated test structure of lines with 140 nm pitch. The line pattern is just visible in flat-noise, and notch-filtered SIM but overshadowed by the noise pattern with uneven distribution of noise over spatial frequencies in true-Wiener SIM. Scale bar 1 μm.
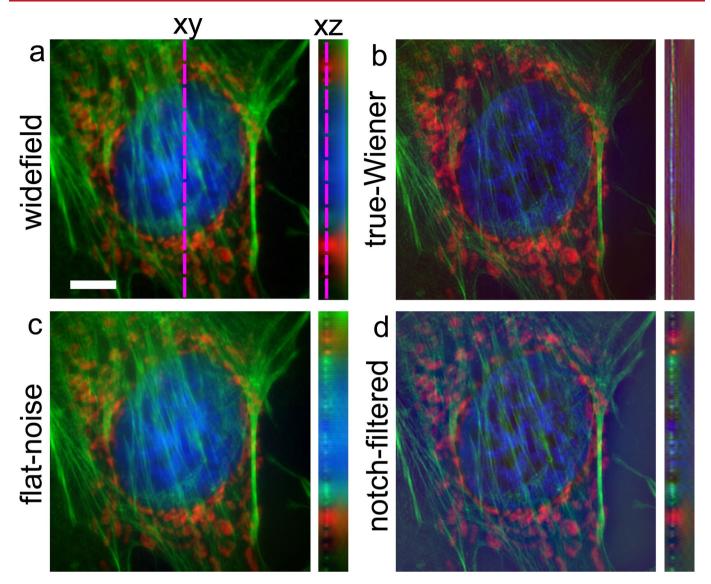
Extended Data Fig. 5 | Noise-controlled 2D-SIM of synaptonemal complex. a–d, Widefield, and true-Wiener, flat-noise and notch-filtered SIM reconstructions of the mCherry-CSYCP3 protein in the synaptonemal complex. **e–h**, Line profiles along the lines indicated in (**b**). The SIM reconstructions reveal the two cable sub-structure with a line distance of around 200 nm, flat-noise SIM has less contrast but shows smoother lines and no background noise structure. Scale bar 3 μm.
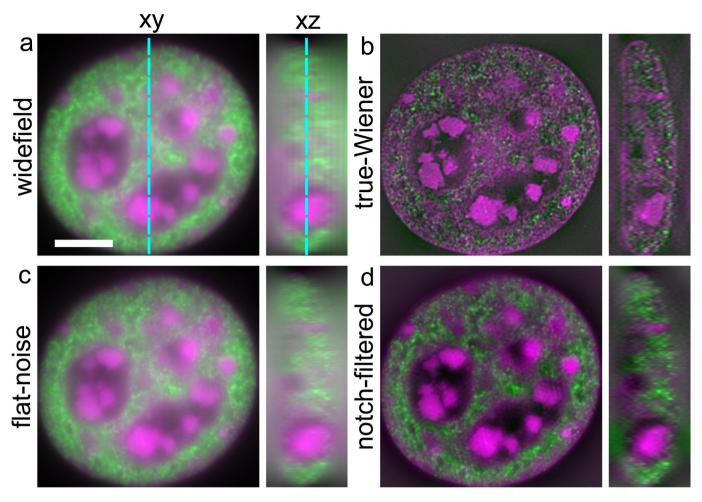
Extended Data Fig. 6 | Cross-sections in xy and yz-planes of 3D-reconstructions of tubulin (green) and noise fraction maps (magenta) for different camera exposure times. a, Widefield, (**b–d**) state-of-the-art SIM for low, medium and high regularization, (**e**) true-Wiener SIM, (**f**) flat-noise SIM, and (**g**) notch-filtered SIM. The dashed lines in (**a**) indicate the location of the xz and xy slices. Scale bar 3 μm.
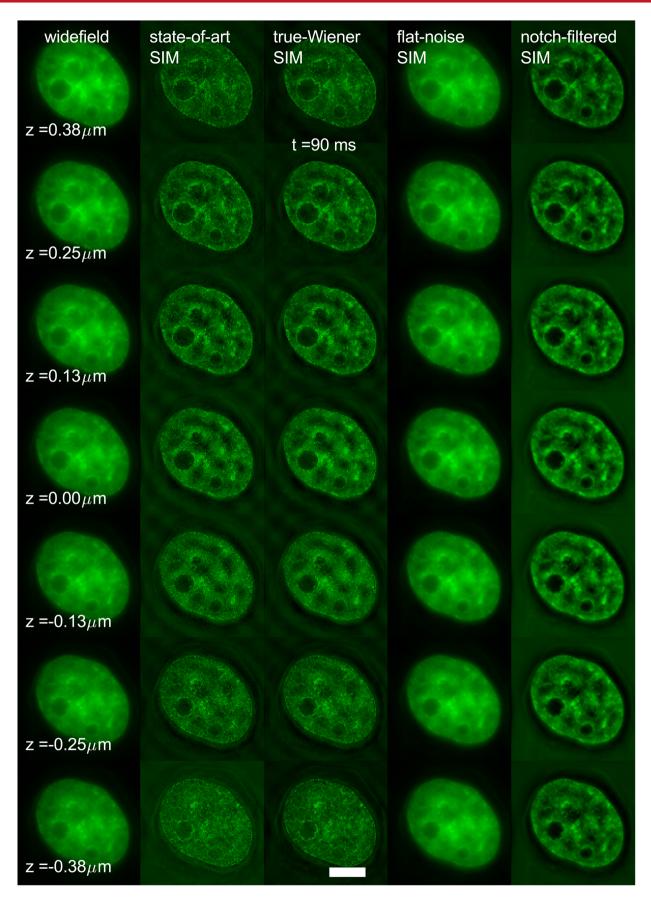
Extended Data Fig. 7 | Widefield and noise-controlled 3D-SIM reconstructions of a 100 nm bead layer sample. a,b, Widefield, (**c,d**) true-Wiener SIM, (**e,f**) flat-noise SIM, (**g,h**) notch-filtered SIM. The white box in (**c**) indicates the insets (**b,d,f,h**). **i,j**, *SSNR* of the SIM reconstructions without (**i**) and with (**j**) notch filtering. The data is averaged over rings in Fourier space and the plot is on a logarithmic scale according to $\log_{10}(1+SSNR)$. The red line indicates the (ring averaged) support of the SIM-OTF, the white line indicates the $SSNR=5$ region in Fourier space used for the extrapolation of the true-Wiener regularization filter. **k**, FRC curves for SIM obtained from 4 repeated acquisitions of the bead layer sample. The FRC resolution is 106.3 ± 0.5 nm, very close to the extended SIM diffraction limit $1/(2NA/\lambda + 2/p) = 99$ nm for the estimated pattern pitch $p = 416$ nm, consistent with the relatively high signal level (peak pixel intensities above 10^4 detected photons) and the broad support of *SSNR* above one in spatial frequency space. Scale bar (**a,c,e,g**) 3 μm, scale bar (**b,d,f,h**) 1 μm.

Extended Data Fig. 8 | Widefield and 3D noise-controlled SIM reconstructions of a bovine pulmonary artery endothelial cell. a, Widefield, (**b**) true-Wiener SIM, (**c**) flat-noise SIM, (**d**) notch-filtered SIM (BPAEC, red channel: mitochondria labeled with Alexa Fluor 594, green channel: actin labeled with FITC, blue channel: DNA labeled with DAPI). Scale bar 5 μm.

Extended Data Fig. 9 | Widefield and 3D noise-controlled SIM reconstructions of a mouse C127 cell. a, Widefield, (**b**) true-Wiener SIM, (**c**) flat-noise SIM, (**d**) notch-filtered SIM (magenta channel: DNA labeled with DAPI, green channel: H3K4me3 labeled with Alexa Fluor 488, blue channel: DNA labeled with DAPI). Scale bar 5 µm.

Extended Data Fig. 10 | Widefield, state-of-the-art SIM and noise-controlled 3D-SIM reconstructions for one timeframe of the 15 timeframe, 7-layer dataset of H2B-GFP histone in a live HeLa cell. Scale bar 6 μm.

nature research

Corresponding author(s): S. Stallinga

Last updated by author(s): Apr 16, 2021

Reporting Summary

Nature Research wishes to improve the reproducibility of the work that we publish. This form provides structure for consistency and transparency in reporting. For further information on Nature Research policies, see our Editorial Policies and the Editorial Policy Checklist.

Statistics

For all statistical analyses, confirm that the following items are present in the figure legend, table legend, main text, or Methods section.

n/a	Confirmed	
☒	☐	The exact sample size (*n*) for each experimental group/condition, given as a discrete number and unit of measurement
☒	☐	A statement on whether measurements were taken from distinct samples or whether the same sample was measured repeatedly
☒	☐	The statistical test(s) used AND whether they are one- or two-sided *Only common tests should be described solely by name; describe more complex techniques in the Methods section.*
☒	☐	A description of all covariates tested
☒	☐	A description of any assumptions or corrections, such as tests of normality and adjustment for multiple comparisons
☐	☒	A full description of the statistical parameters including central tendency (e.g. means) or other basic estimates (e.g. regression coefficient) AND variation (e.g. standard deviation) or associated estimates of uncertainty (e.g. confidence intervals)
☒	☐	For null hypothesis testing, the test statistic (e.g. *F*, *t*, *r*) with confidence intervals, effect sizes, degrees of freedom and *P* value noted *Give P values as exact values whenever suitable.*
☒	☐	For Bayesian analysis, information on the choice of priors and Markov chain Monte Carlo settings
☒	☐	For hierarchical and complex designs, identification of the appropriate level for tests and full reporting of outcomes
☒	☐	Estimates of effect sizes (e.g. Cohen's *d*, Pearson's *r*), indicating how they were calculated

Our web collection on statistics for biologists contains articles on many of the points above.

Software and code

Policy information about availability of computer code

Data collection	Matlab code is available at https://github.com/qnano/simnoise, and is developed under Matlab2018b. ImageJ code for 2D-SIM is available at https://github.com/fairSIM, and operates under ImageJ version 1.53. SIMcheck version 1.1 available at https://github.com/MicronOxford/was used for comparison in the data analysis.
Data analysis	Matlab code is available at https://github.com/qnano/simnoise, and is developed under Matlab2018b. ImageJ code for 2D-SIM is available at https://github.com/fairSIM, and operates under ImageJ version 1.53. SIMcheck version 1.1 available at https://github.com/MicronOxford/was used for comparison in the data analysis.

For manuscripts utilizing custom algorithms or software that are central to the research but not yet described in published literature, software must be made available to editors and reviewers. We strongly encourage code deposition in a community repository (e.g. GitHub). See the Nature Research guidelines for submitting code & software for further information.

Data

Policy information about availability of data

All manuscripts must include a data availability statement. This statement should provide the following information, where applicable:
- Accession codes, unique identifiers, or web links for publicly available datasets
- A list of figures that have associated raw data
- A description of any restrictions on data availability

All raw image data is available at https://doi.org/10.4121/12942932 .

Field-specific reporting

Please select the one below that is the best fit for your research. If you are not sure, read the appropriate sections before making your selection.

☒ Life sciences   ☐ Behavioural & social sciences   ☐ Ecological, evolutionary & environmental sciences

For a reference copy of the document with all sections, see nature.com/documents/nr-reporting-summary-flat.pdf

Life sciences study design

All studies must disclose on these points even when the disclosure is negative.

Sample size	One imaging experiment (zyxin dataset) was repeated 10x for experimental assessment of noise level from the variances. This sample size (n=10) was sufficient as typically further averaging over on the order 10^2 pixels was done, giving errors ~1/sqrt(10^3), i.e. of just a few percent at worst.
Data exclusions	No data was excluded
Replication	Imaging experiments other than the zyxin dataset were not replicated as no additional control of noise statistics was needed.
Randomization	The order of the n=10 imaging experiment or subdivision in groups has no statistical meaning.
Blinding	n.a. as no group allocation was performed

Reporting for specific materials, systems and methods

We require information from authors about some types of materials, experimental systems and methods used in many studies. Here, indicate whether each material, system or method listed is relevant to your study. If you are not sure if a list item applies to your research, read the appropriate section before selecting a response.

Materials & experimental systems

n/a	Involved in the study
☐	☒ Antibodies
☐	☒ Eukaryotic cell lines
☒	☐ Palaeontology and archaeology
☒	☐ Animals and other organisms
☒	☐ Human research participants
☒	☐ Clinical data
☒	☐ Dual use research of concern

Methods

n/a	Involved in the study
☒	☐ ChIP-seq
☒	☐ Flow cytometry
☒	☐ MRI-based neuroimaging

Antibodies

Antibodies used	Mouse mAb anti-Tubulin clone DM1A, Sigma-Aldrich / Merck, Cat # T6199, 1:1000 Rabbit pAb anti-H3K4me3, Active Motif, Cat # 39159, 1:500 Donkey anti-Mouse IgG (H+L) Alexa Fluor 488, Thermo Fisher Scientific, Cat # A32766, 1:1000 Goat anti-Rabbit IgG (H+L) Alexa Fluor 488, Thermo Fisher Scientific, Cat # A32731, 1:1000
Validation	Mouse mAb anti-Tubulin: validated by the manufacturer (antibody enhanced validation (https://www.sigmaaldrich.com/technical-documents/articles/biology/antibody-enhanced-validation.html) Rabbit pAb anti H3K4me3: validated by the manufacturer (https://www.activemotif.com/catalog/details/39159)

Eukaryotic cell lines

Policy information about cell lines

Cell line source(s)	C127:LT ATCC CRL-1804 HeLa: ATCC CCL-2 U2Os: was kindly provided by M.W. Paul originaly and used in previously in : Sánchez, H., Paul, M.W., Grosbart, M., van Rossum-Fikkert, S.E., Lebbink, J.H.G., Kanaar, R., Houtsmuller, A.B., and Wyman, C. (2017). Architectural plasticity of human BRCA2-RAD51 complexes in DNA break repair. Nucleic acids research 45, 4507-4518. And: Legerstee, K., Geverts, B., Slotman, J.A., and Houtsmuller, A.B. (2019). Dynamics and distribution of paxillin, vinculin, zyxin and VASP depend on focal adhesion location and orientation. Scientific reports 9, 10460.

Authentication	Cell lines was not authenticated
Mycoplasma contamination	C127 and HeLa: Cell lines was not tested for contamination. U2Os: Cells tested negative for mycoplasma
Commonly misidentified lines (See ICLAC register)	None used.